Additive Manufacturing 105 (2025) 104785

Contents lists available at ScienceDirect

Additive Manufacturing

journal homepage: www.elsevier.com/locate/addma

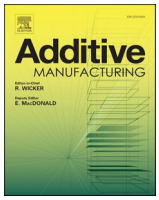

Microstructure tailoring of a wire-arc DED processed Ti6242 alloy for high damage tolerance performance

Farhana Zakir [a], Abdul Khadar Syed [a,*], Xiang Zhang [a,*], Alec E. Davis [b], Vivek K. Sahu [b,1], Armando E. Caballero [c], Romali Biswal [c,2], Philip B. Prangnell [b], Stewart Williams [c]

[a] Centre for Manufacturing and Materials, Coventry University, CV1 5FB, UK
[b] Department of Materials, University of Manchester, M13 9PL, UK
[c] Welding Engineering and Laser Processing Centre, Cranfield University, MK43 OAL, UK

ARTICLE INFO

Keywords:
Additive manufacturing
WAAM
Hammer peening
Fatigue crack growth
Titanium alloys

ABSTRACT

This paper examines the effects of interpass hammer peening and post-process β annealing on the tensile properties, high-cycle fatigue, and fatigue crack growth behaviour of the titanium alloy Ti-6Al-2Sn-4Zr-2Mo-0.1Si (Ti6242), processed via wire-arc directed energy deposition (w-DED, also known as WAAM). A major challenge in additive manufacturing of titanium alloys is the development of a coarse columnar grain structure under standard build conditions, leading to significant anisotropy and variability in mechanical properties. This study demonstrates that interpass peening effectively refines the grain structure by inducing recrystallization, resulting in isotropic properties and increased strength without compromising fatigue crack growth resistance. Additionally, post-deposition annealing above the β-transus temperature (β annealing) significantly reduces the fatigue crack growth rate by an order of magnitude through microstructural refinement. The formation of coarse single-variant lamellar colonies promotes crack path branching and deviation, enhancing fatigue crack growth performance. Combining in-process grain refinement via peening with post-process β annealing further increases the threshold stress intensity factor by 2.5 times. These improvements provide substantial benefits for damage-tolerant design principles.

1. Introduction

The titanium alloy Ti-6Al-2Sn-4Zr-2Mo-0.1Si (Ti6242) is a near-α alloy that offers an excellent combination of tensile strength, fracture toughness, and creep resistance up to a maximum temperature of 560 °C. It is commonly used in aerospace engine components that require high mechanical performance at elevated temperatures, beyond the capabilities of alloys like Ti-6Al-4V (Ti64) [1,2]. Due to the increasing temperatures in engine cores, Ti6242 is now being considered for applications in engine pylons, where damage tolerance is a critical design consideration. Traditionally, producing mass-effect components from semi-finished forged and rolled products requires extensive machining, leading to a buy-to-fly ratio (the mass ratio of raw material to final finished part) of 12–25:1 for titanium aerospace parts made by conventional manufacturing processes [3]. In contrast, additive manufacturing (AM) has the potential to reduce this ratio to 1.2:1 [4]. Among the AM processes suitable for producing large-scale parts, wire-arc directed energy deposition (w-DED), also known as wire and arc additive manufacturing (WAAM), has gained increasing interest from the aerospace and other industries due to its high deposition rate, low cost, and nearly 100 % utilization of feedstock materials [5].

In general, AM processes involve high heat inputs and repeated heating and cooling cycles, resulting in unique solidification conditions compared to conventional wrought and casting methods. The positive thermal gradient at the solidification front within the heated melt pool, combined with the narrow solidification range of titanium alloys and the absence of artificial grain refiners, typically prevents free nucleation. Instead, it promotes columnar-dendritic growth through epitaxial

* Corresponding authors.
E-mail addresses: abdul.syed@coventry.ac.uk (A.K. Syed), xiang.zhang@coventry.ac.uk (X. Zhang).
[1] Currently at: Department of Fuel, Minerals and Metallurgical Engineering, India Institute of Technology-Indian School of Mines Dhanbad, Jharkhand, India.
[2] Currently at: The Manufacturing Technology Centre, Coventry, UK.

https://doi.org/10.1016/j.addma.2025.104785
Received 1 January 2025; Received in revised form 8 April 2025; Accepted 10 April 2025
Available online 11 April 2025

nucleation at the fusion boundary. In most AM processes involving titanium, this results in continuous, competitive columnar dendritic growth across multiple repeated layers, leading to large columnar β grains and a strong < 001 > // ND fiber texture aligned with the average solidification direction, which is usually close to the build direction [6]. Due to the large melt pool formed by the high energy input and thicker layer deposition in high deposition rate AM processes, titanium alloys such as Ti64 and Ti6242 typically develop very coarse (centimeter--scale) columnar β grain structures in the as-built condition. This coarse grain structure introduces micro-texture heterogeneity in the α-β transformation microstructure, which can result in significant scatter and anisotropy in both the static and dynamic mechanical properties [7,8].

Various efforts have been made to refine columnar grains, such as adding growth restrictors like boron [9], carbon [10] or copper [11], or using grain inoculants such as TiAlNb [12], ZrN [13] and TiN [13]. While *in situ* alloying can effectively suppress columnar grain growth, these trace additions also induce other metallurgical changes that negatively impact the mechanical properties [12,13]. Another approach involves modifying the solidification conditions, where the specific energy density and preferential grain growth direction can be controlled by increasing the wire feed speed, which leads to grain refinement [14]. However, this must be carefully balanced with the potential risks to deposition stability and part geometry [15]. A third approach is to promote in-situ recrystallization of the β phase by applying in-process (interpass) deformation through rolling or peening. This method leverages the layer-wise nature of AM. Previous research has shown that sufficient deformation by rolling or peening, combined with cyclic re-heating to temperatures exceeding the β transus, can induce new β orientations during the deposition of successive layers, disrupting large-scale columnar grain growth [16,17]. In Ti64, this approach has been shown to produce a refined equiaxed β grain structure, resulting in a weaker and more homogeneous α transformation texture and microstructure [6]. As a result, near isotropic tensile properties have been reported [17–19]. However, research on WAAM using the higher-temperature Ti6242 alloy has thus far focused solely on microstructure modification via interpass peening [6], and its material properties have not yet been reported.

Several studies have investigated the static properties of AM built Ti6242 deposits [20–24]. Much of the published work has primarily focused on powder bed Ti6242, its associated martensitic α′ microstructure, and its decomposition. The martensitic microstructure in as-built Ti6242 produced via laser powder bed fusion (L-PBF) resulted in high strength but lower ductility and significant anisotropy in tensile properties. When L-PBF Ti6242 samples were subjected to low temperature tempering heat treatments, ductility improved at the expense of reduced strength due to the complete transformation of α′ to α [24]. In contrast, β annealing of L-PBF Ti6242 has been reported to produce a coarser lamellar microstructure, resulting in a 30 % decrease in strength but a significant increase in elongation, along with anisotropy in elongation [21]. Electron Beam Powder Bed Fusion (EB-PBF) manufactured Ti6242 subjected to hot isostatic pressing (HIPing) in the temperature range of 850–1050°C (i.e., below and slightly above the β transus temperature) resulted in reduced yield strength and increased ductility due to reduced porosity and the decomposition of martensite [22].

High cycle fatigue (HCF) strength in titanium alloys decreases in the order of bimodal, lamellar and equiaxed microstructure [25]. Hagiwara et.al [26] studied the relationship between microstructures and HCF properties of hot-rolled Ti6242. The material was systematically heat treated to produce different microstructural morphologies. The results confirmed that HCF strength was highly dependent on the α lath width. The bimodal microstructure with an α size of 5 μm exhibited the highest HCF strength, followed by an equiaxed α microstructure with a grain size of approximately 10 μm, and then the acicular α microstructure and the equiaxed α microstructure with a grain size of about 15 μm [26]. Although the Ti6242 alloy is designed for high temperature applications, it has been reported that a reduction in fatigue life at higher temperatures is mainly caused by increased oxidation and, in some cases, by creep [27]. Typically, Ti6242 develops a variety of microstructure depending on the AM process and associated cooling rates. Research on the fatigue performance of AM built Ti6242 is limited. HCF properties of a powder feed DED Ti6242 were studied at 450°C and showed anisotropic fatigue strength [28]. At higher applied stress, samples loaded perpendicular to the material build direction exhibited longer fatigue life due to higher yield strength in this orientation, whereas shorter fatigue life was observed under lower applied stress. However, the authors did not present any discussions on the observed anisotropy in fatigue strength.

The damage tolerance design principle requires a thorough understanding of the fatigue crack growth (FCG) behavior of materials used in safety-critical applications. The fatigue crack growth rate (FCGR) is a crucial material property for predicting the fatigue life of components. The FCGR of an alloy depends on extrinsic factors, such as loading and environmental conditions, as well as intrinsic factors, including microstructural features and material composition.

In titanium alloys, a lamellar colony microstructure, typically found in cast products, provides enhanced resistance to crack growth [29,30]. A study reported in [31] concluded that the FCGR of conventionally manufactured Ti6242 decreased with a reduction in the volume fraction of the primary α phase (α_p). An increase in α lath width and the presence of secondary α phase (α_s) after heat treatment resulted in crack path deflections, reducing the crack growth rates. In another study [32], the FCGR of bimodal and lamellar microstructures was compared. The bimodal microstructure exhibited a lower FCGR and a lower fatigue crack growth threshold (ΔK_{th}). The high resistance to FCG in the lamellar microstructure was attributed to crack tortuosity, where the boundaries of lamellar colonies caused crack path deflections. In contrast, in the bimodal microstructure, fatigue cracks propagated by cleaving the large primary α grains.

Although none of the studies mentioned above have addressed the fatigue crack growth behaviour of AM Ti6242 alloys, research on wrought materials shows that crack growth rates in similar titanium alloys, such as Ti64, are highly sensitive to microstructural conditions and texture heterogeneity. Additionally, for airframe applications like engine pylons, a β annealing treatment is often used to increase damage tolerance. This heat treatment produces a coarse lamellar single α-variant colony microstructure, which is very effective at crack deflection. It also enhances closure effects, reducing the effective local stress intensity range (ΔK) at the crack tip, which can reduce crack growth rates by orders of magnitude. However, this requires careful control of the β grain size to be fully effective.

In summary, to date, nearly all research on grain refinement in AM titanium alloys has focused on the industry-standard Ti64 alloy. Reports on the properties of Ti6242 produced by AM are limited to tensile test data from materials manufactured using powder bed fusion processes, with only one published study investigating its high-cycle fatigue (HCF) behavior [33]. However, since the damage tolerance design philosophy is essential for many safety-critical parts in commercial aircraft, understanding fatigue crack growth properties is also crucial. Therefore, this study aims to systematically explore the potential for microstructure tailoring to improve the anisotropy and fatigue crack growth behavior of Ti6242 alloy produced by the w-DED process. This is achieved by combining in-process deformation (via hammer peening) with post-deposition heat treatment. Three different conditions have been studied: i) standard w-DED material with a conventional columnar prior β grain structure, ii) w-DED with interpass hammer peening leading to refined prior β grains, and iii) w-DED with interpass peening followed by β annealing heat treatment. The tensile, HCF, and FCGR test results for these conditions are analyzed and compared with those of conventional wrought material and other AM-built counterparts. Discussions are supported by detailed microstructure analysis using scanning electron microscopy (SEM) combined with electron backscatter diffraction

(EBSD).

2. Experimental

2.1. Wire DED Ti6242 manufacturing

Three walls were built using single pass w-DED process and a Ti6242 alloy wire as the feedstock. The wall geometry is shown in Fig. 1a. A baseline wall was built using the standard process parameters provided in Table 1. The chemical composition of the Ti6242 wire (AMS 4975 N) is given in Table 2. The other two walls were built using the same process parameters, with the addition of interpass hammer peening applied to each material layer using a pneumatic RRH06P Atlas Copco machine hammer peening (MHP) tool with a 10 mm radius spherical head. It is operated by a robot with an impact energy of 6 J and translation rate of 10 mm/sec, which generated a peening pitch of 0.4 mm. It is worth highlighting that the interpass hammering peening was applied only to refine the prior β grains. In our previous study [34], a systematic experimental investigation was carried out using contour method to determine the influence of peening on residual stresses in WAAM Ti64 walls. The results showed that the application of peening had little influence on residual stresses in the walls. Both walls were built with thermal monitoring to ensure a consistent interpass temperature of 60 ± 20 °C on the top surface at the centre of the wall before peening was applied. One of the two peened walls was subjected to post-build standard β annealing heat treatment to 1050 °C at 0.3 °C/s for 30 minutes, followed by cooling at ~ 0.1 °C/s.

2.2. Microstructure and EBSD analysis

Microstructure analysis was conducted on samples sectioned from the wall centres in the WD-ND and ND-TD planes (Fig. 1a) using optical light microscope and scanning electron microscopes (SEM). Metallographic preparation involved silicon carbide papers with reducing grit size down to 2500, followed by polishing with diamond suspension to a 3 μm finish. The final polishing step was carried out using colloidal silica with a 0.05 μm particle size. The optical samples were etched with Kroll's Reagent. For α lath width measurements, multiple secondary electron SEM images were taken across the WD-ND plane and then processed using Image-J software by the line intersection method, according to ASTM E112 standard [35].

EBSD maps were acquired in the ND-TD plane using a Thermo Fisher Apreo C, field emission gun SEM, equipped with an Oxford Instruments' Symmetry 2 EBSD detector. The acquisition was done with an accelerating voltage of 20 kV and a beam current of 51 nA at an indexing rate of 1800 Hz, with a step size of 10 μm. EBSD maps were processed and β grain size data were extracted using Oxford instruments' AZtecCrystal software. The EBSD maps are shown in inverse pole figure (IPF) colouring with the orientation reference parallel to ND. Texture data is displayed in contoured pole figures scaled in multiples of random density (MRD). The parent β phase maps were reconstructed from the α phase data using the software developed by Davies and Wynne [36] with a maximum disorientation of 2° from a particular α variant accepted, and up to a 3° divergence from the Burgers orientation relationship (BOR) as a part of the same parent β grain.

Table 1
Process parameters used for the w-DED Ti6242 deposition.

Power	Current	180 A
	Arc voltage	23 V
Speed	Torch travel seed	0.3 m/min
	Wire feed speed	2 m/min
Flow rate	Plasma gas	0.8 l/min
	Shielding gas (Argon)	70 l/min

2.3. Mechanical testing

Flat, dog-bone shaped, tensile specimens (Fig. 1b), 5 mm thick and 6 mm wide, were extracted using wire electric discharge machining (W-EDM) from the walls in two orientations: horizontal (H) and vertical (V), corresponding to the loading axis being in parallel or perpendicular to the deposited layers (Fig. 1). The sample size (Fig. 1b) and testing procedure follow the ASTM E8 standard [33]. Tensile testing was performed on an Instron electromechanical test machine with 100 kN load cell, at a crosshead speed of 2 mm/min, at room temperature. Extensional deformation was measured using a laser non-contact video extensometer over a gauge length of 25 mm. Two specimens were tested for each process condition and material orientation. The results are presented in terms of the engineering stress and strain relationship.

High cycle fatigue (HCF) tests by rotating bending load were conducted using round dog-bone specimens with two material orientations (Figs. 1c, 1a). To produce cylindrical dog-bone shaped samples, 8 mm diameter rods were extracted from the wall. The rods were subsequently machined to the HCF specimen geometry shown in Fig. 1c. Prior to testing, the sample gauge section was polished using SiC papers (up to 2500 grit) to reduce the average surface roughness. Two to three

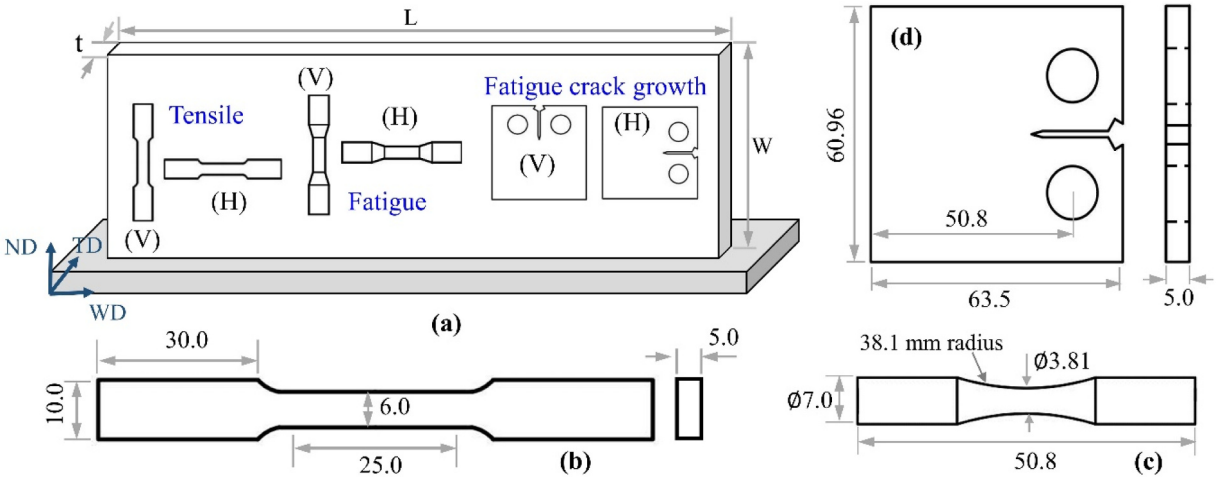

Fig. 1. (a) one of the w-DED walls with sample extraction plan for tensile, high cycle fatigue, and fatigue crack growth tests, showing the definition of the vertical (V) and horizontal (H) test specimens. Sample reference frame, WD = welding direction, TD = transverse (thickness) direction, ND = normal direction. Wall dimensions: L = 240, W = 73–105, t = 10. Geometry and dimensions of (b) tensile specimen, (c) high cycle fatigue specimen, (d) compact tension C(T) specimen (unit: mm).

Table 2
Chemical composition of Ti6242 wire feedstock.

	Al	Sn	Zr	Mo	Si	Cu	N	O	C	Fe	Mn	B	Ti
wt%	6.0	2.0	3.9	2.0	0.09	< 0.02	0.003	0.12	0.005	0.03	< 0.02	< 0.003	Balance

samples were tested at each stress level. Tests were conducted at 50 Hz loading frequency and a cyclic load ratio −1. After failure, all the samples were analysed under the SEM to identify the crack initiation sites and mechanisms.

For fatigue crack growth tests, the compact tension (CT) samples (Fig. 1d) were extracted using W-EDM in either the horizontal (H) or vertical (V) orientation, where the crack growth path was either parallel or normal to the deposited layers (Fig. 1a). The samples were designed and tested according to the ASTM E647 standard [37]. Prior to testing, the anticipated crack path was polished to improve crack visibility. An Instron ElectroPuls machine with a 3 kN load cell was used for the test, employing a sinusoidal waveform and a cyclic load ratio 0.1. Crack length extension was measured using a travelling microscope with 7 × objective magnification and an accuracy of ± 0.01 mm. Each test was conducted in two stages. First, a test of decreasing stress intensity factor range (ΔK) was conducted using the load shedding procedure outlined in ASTM E647 to obtain the threshold value of the stress intensity factor range (ΔK_{th}). The test was conducted at a 30 Hz frequency until the crack growth rate decreased to below the value of 10^{-10} m/cycle, where the applied ΔK was deemed to have reached its threshold value ΔK_{th}. Subsequently, a constant amplitude load test was conducted at 20 Hz loading frequency until the crack became unstable leading to final fracture of the specimen. The fatigue crack growth rates (da/dN) were calculated from a measured relationship of crack length vs. load cycles using a seven-point incremental polynomial method for most of the data points. A secant method was used to find the threshold and the cyclic fracture toughness (i.e., the first three and the last three data points of the crack length vs. load cycle curve), as recommended by the ASTM E647 standard. Fitted relationship of da/dN vs. ΔK was then obtained, where ΔK was calculated using the following equation in ASTM E647 [37]:

$$\Delta K = \frac{\Delta P}{B\sqrt{W}} \frac{(2+\alpha)}{(1-\alpha)^{\frac{3}{2}}}(0.886 + 4.64\alpha - 13.32\alpha^2 + 14.72\alpha^3 - 5.6\alpha^4) \quad (1)$$

where, P is the applied load, B is the thickness of the C(T) sample, W the

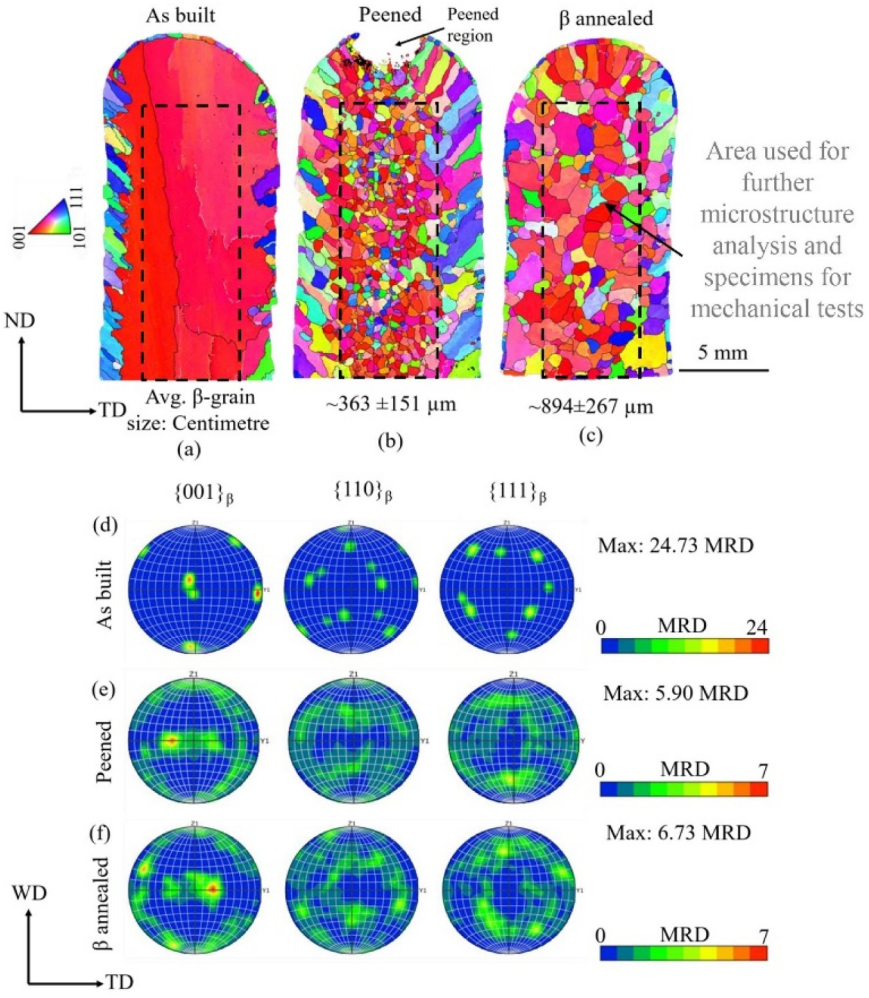

Fig. 2. Reconstructed β-phase EBSD maps from ND-TD plane (on top of the walls) for: (a) as-built, (b) peened, (c) peened + β annealed. In (b) the unindexed region at the top of the wall, indicated with an arrow, reflects the local plastic deformation zone caused by peening. The area marked with dashed lines was used for further microstructure analysis and for extracting mechanical test samples by excluding near surface regions with extreme grain size. Pole figures show the corresponding β phase textures from the reconstructed maps: (d) as-built, (e) peened, (f) β annealed. Note: the contour intensity range in (d) is larger than that of (e) and (f).

distance from the loading line to the sample edge, a the crack length, and $\alpha=a/W$.

After failure, surface roughness of the CT samples were measured using a high-resolution 3D optical Alicona Infinite Focus metrology system. The measurement was carried out at a distance of 5 mm from the EDM notch. The surface roughness was represented using the areal surface roughness parameter S_a, which was determined over a measurement area of 3×5 mm^2.

3. Results and discussion

3.1. Microstructure characterization

3.1.1. β Grain structures

Before mechanical testing, the microstructures of the 3 sample conditions (i.e., standard WAAM, peened, and peened plus β annealed) were characterized to investigate their β grain structures and transformation microstructure features that might influence their mechanical performance. Reconstructed β phase EBSD maps comparing the β grain structures for the different sample conditions along with their corresponding textures, displayed as $\{001\}_\beta$, $\{110\}_\beta$, $\{111\}_\beta$ pole figures, are depicted in Fig. 2. In the standard sample (Fig. 2a), highly textured, large columnar β grains, on the order of centimetres along the build direction can be seen, which is typical of the WAAM process [6]. The EBSD map from this sample encompasses only a few very large columnar grains present in the core of the wall with a very strong $\langle 001 \rangle_\beta$ // ND fibre texture, giving a maximum pole intensity of 24.73 MRD (shown in Fig. 2d). It has been widely reported that such coarse-columnar β grains form due to the low constitutional undercooling in the WAAM process with titanium alloys that exhibit low solute partitioning [38,39]. The outer thin 'casing' of finer columnar β grains seen in Fig. 2a has been reported previously and is caused by the thermal gradient tilting strongly away from the $\langle 001 \rangle_\beta$ preferred growth direction of the core ND-aligned grains towards the wall surfaces, due to the curved shape of the fusion boundary which is convex in the ND-TD plane [14]. This misalignment of the thermal gradient away from ND towards the wall surfaces (TD) favours the growth of other, better aligned dendrite orientations, that are formed by growth faults (e.g. twinning) or from dendrite fragments [14], and are also be favoured with titanium alloys containing elements like Mo which partition more strongly than V and Al [6,40]. However, in the current test programme the surface was machined off to produce the tensile and C(T) samples, such that the mechanical properties measured were only influenced by the core wall microstructure.

From Figs. 2b and 2c, it is apparent that the application of interpass peening has resulted in successful refinement of the β grain structure, reducing its size from centimetres in the as-built condition to about 360 μm after peening. The grains have also become more equiaxed and less textured. There is again a different surface region where the grain size is coarser and starts to become columnar again towards the wall surfaces tilted to approximately 45° from ND. This has occurred because the spherical peening tool was applied to the curved top bead along the wall centreline. The extent of local deformation below the peening tool position can be inferred from the un-indexed region in the EBSD map, shown shaded on the top layer in Fig. 2b. In other words, high levels of grain refinement were only observed where sufficient strain was imparted to cause recrystallization, and this did not extend fully to the wall surfaces (Fig. 2b). In Fig. 2c it can be further seen that this recrystallized β grain structure has coarsened significantly during the 1050 °C for 30-minutes β annealing treatment to a grain size of about 800 μm but is still approximately equiaxed and has become more uniform across the wall width. For the peened conditions, the grains at the edges of the walls were machined off during the manufacturing the tensile and C(T) samples, and therefore, the refined grains at the edge of the wall did not influence the mechanical properties.

From 'stop-action' studies it has been previously shown that the subsurface deformation induced by the interpass hammer peening results in a steep strain gradient below the peening tool [16]. The intense near-surface strain introduces sufficient dislocations into the microstructure to promote recrystallization during reheating above the β transus, during subsequent passing of the heat source, probably partly due to new β orientations being generated during β regrowth [41]. Overall, this leads to the wide scale β grain refinement seen in Fig. 2b. Surprisingly, prior work has revealed that depth of deformation sufficient to cause recrystallization was only about 0.5 mm below the peened surface, which is less than the remelt depth. However, recrystallization was found to already initiate ahead of the melt pool, as the heat source approached, and these new grains grew downwards to a sufficient depth to survive remelting and become the fusion boundary during solidification at the rear of the melt pool. Thus, after peening, the refinement of the grains that form the fusion boundary in each new layer prevents large columnar grains becoming established, as epitaxial regrowth is restricted to a single layer. In a further study, on β recrystallisation in interpass deformed WAAM Ti64, Davis et al. [41] have shown that the intensity of β grain refinement was relatively insensitive to the deformation rate, deformation temperatures, and as-built α+ β microstructure, but strongly depended on the temperature due to the rapid grain growth rate experienced after reheating above the β transus, when there is no longer any α present to pin the grain boundaries [16]. β annealing of the peened wall has similarly led to significant grain growth despite the modest temperature used above the β transus (1050 °C compared to $T_\beta \sim 1000$ °C, [42–44]). Finally, it should be noted that β grain refinement generated by interpass peening led to a much-reduced texture strength with a maximum intensity of 5.9 MRD (Fig. 2e) that only increased marginally to 6.7 MRD in the β annealed sample (Fig. 2f).

Pole figures of the α phase obtained from the centre region of large-area EBSD maps (Fig. 2) are provided in Fig. 3. It can be seen that the α phase, transformed from parent β grains, had a common $< 001 >$ direction aligned close to the material build direction. The corresponding α texture is very strong with a maximum intensity of 13.4 MRD (Fig. 3a). In contrast, much weaker α texture is observed after peening and β annealing treatment with the maximum intensity values of 2.7 and 4.7 MRD, respectively (Figs. 3b and 3c). Peening has introduced more random crystallographic α orientations into the transformation microstructure through the 12 possible α orientations available via BOR. The weaker texture after peening and annealing can also introduce 'harder' low-Schmid-factor orientations in contrast to the 'softer' high Schmid-factor orientations that can be found in columnar-grained structures [16,45].

3.1.2. Transformation microstructures

Optical and SEM images depicting the main features of the α-β transformation microstructures found in the 3 sample conditions are provided in Fig. 4, taken from ND-TD plane metallographic sections. All of the builds contained lamellar α microstructures formed by diffusion-controlled transformation on cooling below the β transus. In the two walls that were not heat treated, heat affected zone (HAZ) bands, can be seen periodically spaced along the build direction (Fig. 4a and b). These bands are more parallel in the standard WAAM build but have an alternating tilt in the peened sample (Fig. 4b), which occurred due to misalignment between the wall centrelines relative to the heat source, when the build table was rotated 180° between depositing each layer in this wall. Similar HAZ bands are commonly observed in most wire-based AM processes with titanium alloys and are particularly prominent in WAAM due to the thicker layer height [46,47]. They form in the temperature gradient under the heat source when the previous layer is reheated to a peak temperature between ~ 800 °C and the β transus (~1000 °C) [46,47]. This results in coarsening of the α laths and greater interphase solute partitioning, which appears as a darker layer in the HAZ band in the as-built and the peened samples. At the top of each HAZ band a thin white etched layer is seen, caused by a finer single α variant lamellar colony microstructure that is formed where the peak

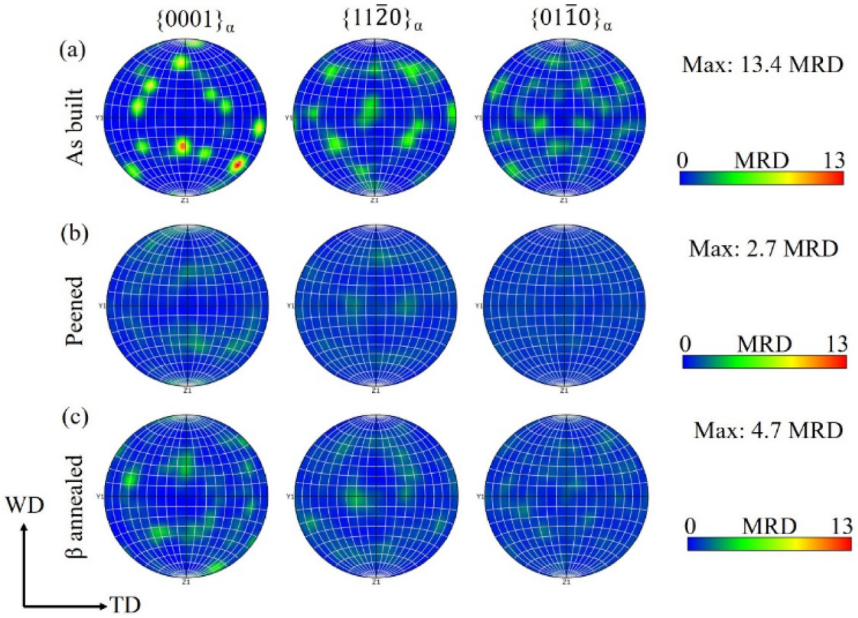

Fig. 3. Pole figures of α phase measured in these conditions: (a) as-built, (b) peened, (c) peened + β annealed.

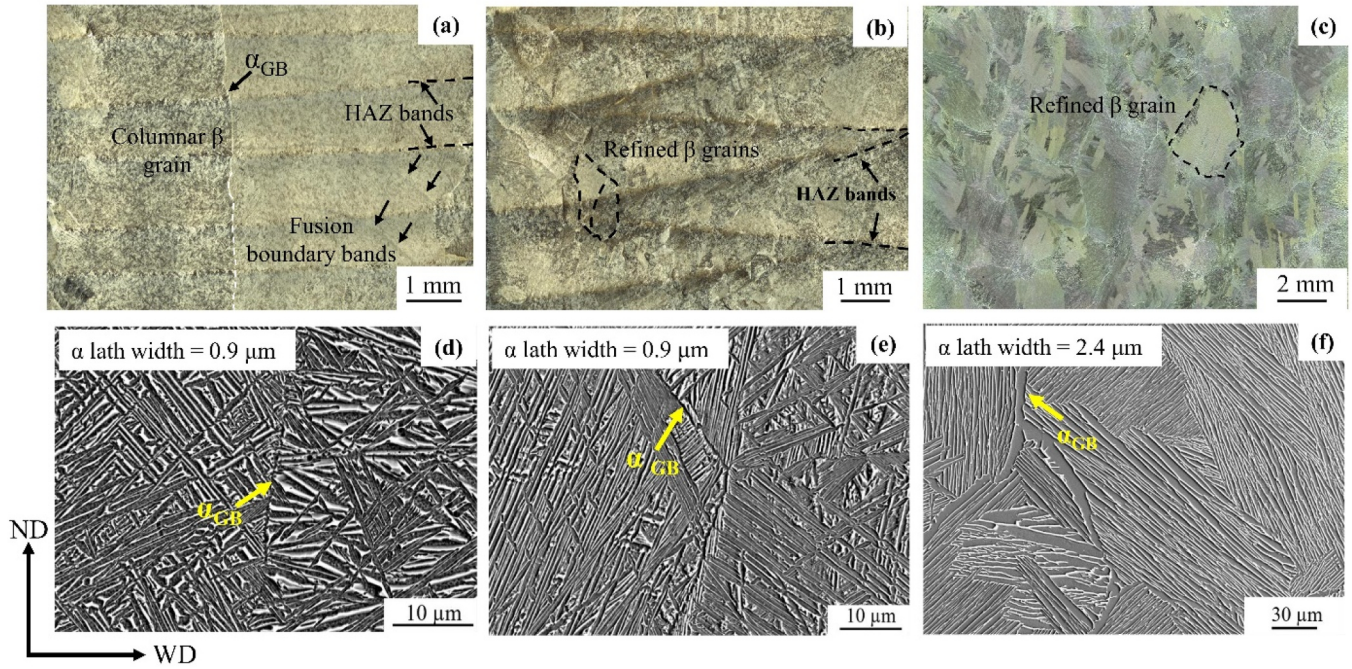

Fig. 4. Optical micrographs along the ND-TD plane of three conditions: (a) as-built, (b) peened, (c) peened + β annealed. The HAZ and fusion boundary bands visible in the as-built and peened samples are indicated in (a) and (b). Secondary electron SEM images showing typical transformation microstructures within the prior β grains: (a) as-built, (b) peened (c) β annealed.

temperature was just below the β transus (~1000°C) when < 5 % α remains and α is sympathetically nucleated from the surviving α plates on cooling [35–37]. The second feature observed in Fig. 4a are narrower etched lines caused by weak fusion boundary solute segregation [47]. In comparison, after the post-build β heat treatment (Fig. 4c), no HAZ or fusion boundary bands are apparent as the whole wall has been uniformly heat treated and retransformed with longer thermal exposure above the β transus, where solute diffusion is relatively rapid. For this microstructure the slower cooling rate has led to a more prominent grain boundary layer of α allotriomorphs (GB_α), which reveals the β grain structure more clearly than in the other walls. The coarse colony microstructure of the β annealed wall is also apparent in Fig. 4c.

Fig. 4d-f show higher magnification secondary electron SEM images of the typical transformation microstructure found within the transformed β grains. The transformation microstructures in WAAM α-β titanium alloys strongly depend on both the cooling rate below the β transus temperature and the extent of reheating during subsequent passes of the heat source as additional layers are added. This reheating can cause coarsening of the average lath width if there is overlap of the HAZ bands, as seen in Fig. 3a [48]. The large heat source and thicker layer deposition associated with the WAAM process result in slower cooling rates of about 30 °C/s [49] compared to other AM processes,

such as laser-PBF, which have cooling rates greater than 10^5 °C/s [49]. Despite this, the cooling rate is still relatively high compared to that of conventionally heat treated parts. As a result, only a narrow single α-variant colony layer forms along the β grain boundaries, with the majority of the β grains transforming into a fine basketweave lamellar α microstructure. This microstructure consists of diffuse interpenetrating colonies of different sub-sets of the α variants permissible by the Burgers Orientation Relationship (BOR) (typically tri-variant), separated by thin films of retained β.

The average α lath width measured for the standard WAAM as-built condition was around 0.9 μm. When interpass peening was used, the refined prior β grains were observed to contain a similar α transformation microstructure with the same average α lath width (0.9 μm). In other words, although peening significantly refined the prior β grains, it did not influence the α lath width or morphology, which forms on a much finer scale and is largely controlled by the cooling rate (Fig. 4e). This is not surprising, as both materials were built under the same process conditions, and thermal monitoring of the interpass temperatures resulted in very similar thermal histories. In contrast, the slow cooling rate (0.1 °C/s) experienced during β annealing after peening led to a substantial increase in α lath width to around 2.4 μm, as well as a thicker grain boundary α allotriomorphic layer (often termed grain boundary α, or GBα). With this low cooling rate, α lath variants were able to grow inward from the GB_α layer on the β grain boundaries until they impinged, forming a microstructure dominated by large single-variant α colonies (Fig. 4f). As the colonies typically meet at the center of the parent β grains, the colony size was approximately half the β grain diameter, around 800 μm. It should be noted that in this case, each colony contains only one α orientation and can be considered to behave mechanically as a single grain, as slip transfer is possible across the lamellar boundaries

3.2. Tensile properties

Fig. 5 presents the engineering stress-strain curves for the three material conditions: as-built (Fig. 5a), peened (Fig. 5b), and β annealed (Fig. 5c). The horizontal and vertical specimen orientations are also shown in the graphs with two repeated tests for each condition. To compare the three conditions, test results with the highest ductility from each condition are plotted in Fig. 5d. The average tensile properties are also listed in Table 3. For the as-built condition, sample orientation had little effect on the yield strength (σ_{YS}) and the ultimate tensile strength (σ_{UTS}) as only marginal anisotropy was observed; horizontal samples exhibits slightly higher strengths by 3 % compared to the vertical samples (Fig. 5a). However, considerable anisotropy and scatter were observed in the elongation-to-failure values; the horizontal samples had much lower values (by 60 %) and larger scatter compared with the vertical samples. A similar trend was also reported in the literature on additively manufactured titanium alloys. The reason or mechanism was thought to be the slip concentration in the thin GB_α single-variant colony

Table 3
Summary of average tensile properties for all test conditions and comparison with literature data of similar materials made by conventional or other AM processes.

Specimens	Orientation	YS (MPa)	UTS (MPa)	Elongation (%)
As-built	Horizontal	880 ± 20	979 ± 6	8 ± 2
As-built	Vertical	855 ± 15	952 ± 9	13 ± 2.0
Peened	Horizontal	942 ± 9	1056 ± 3	10 ± 1
Peened	Vertical	944 ± 13	1065 ± 10	8 ± 0.5
β annealed	Horizontal	826 ± 7	919 ± 1	11 ± 0.5
β annealed	Vertical	823 ± 1	904 ± 7	11 ± 0.5
Cast + ageing [1]		879	984	5
L-PBF [23]		1293 ± 37	1381 ± 79	5.3
EB-PBF [22]		1018 ± 14	1115 ± 18	7.8

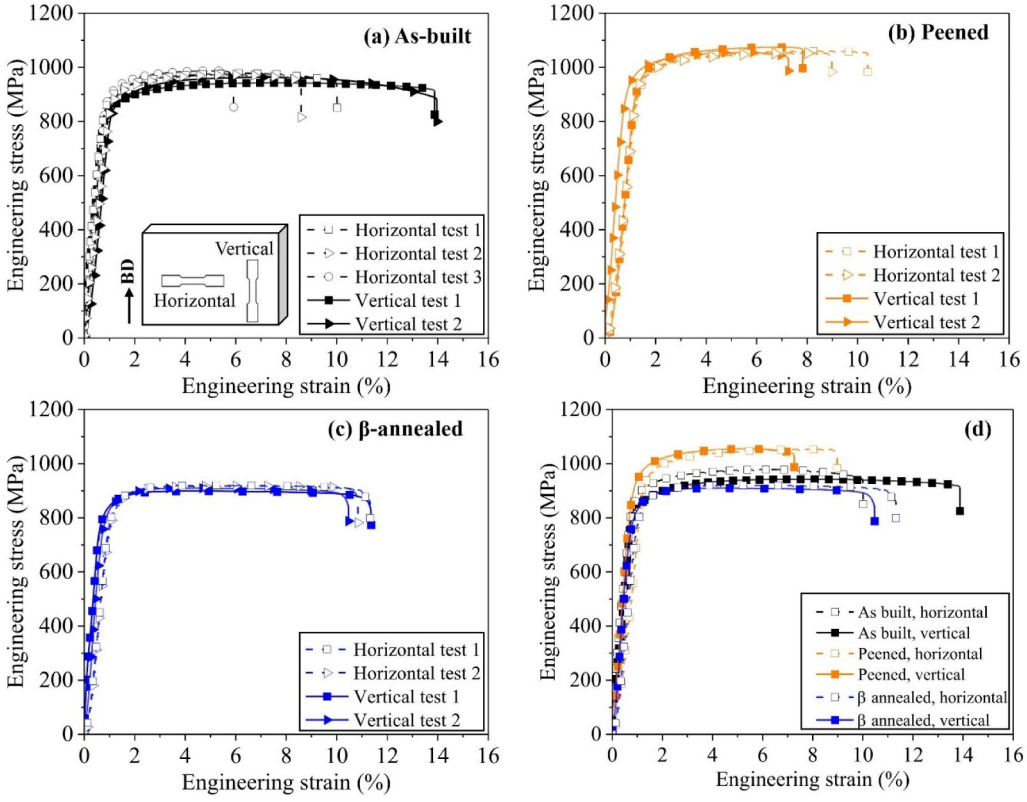

Fig. 5. Engineering stress-strain curves for (a) as-built, (b) peened, (c) β annealed. Comparison of all three conditions is shown is shown in (d); for clarity, only one test data is shown per condition that had the highest elongation.

layers that were developed from the columnar β boundaries, when specimen is transversely loaded [50–52]. This leads to much reduced elongation values in the horizontal samples because with a coarse columnar grain structure, which is oriented along ND plane, it is possible to find a lower resistance shear path within the gauge length, where there is an inclined β grain boundary plane aligned at 45° to the tensile axis through the sample thickness [53]. In comparison, in the vertical (ND direction) samples, the loading axis is parallel to the columnar β grains, so that it is much more difficult to find an easy slip microstructural path through the gauge section that can lead to shear localization [52].

For the grain-refined and weakly textured peened condition, without a post-build heat treatment, two observations can be made based on Figs. 5b, 5d, and Table 3. First, the yield strengths of both sample orientations are higher than those of the as-built condition, with an increase of 7 % in the horizontal samples and 10 % in the vertical samples. The ultimate tensile strength similarly increased by 8 % in the horizontal samples and 12 % in the vertical samples. Second, the anisotropy and scatter in elongation observed in the as-built condition (Fig. 5a) are significantly reduced, indicating near-isotropic behavior. Finally, the post-build heat treatment applied to the β annealed samples, following grain refinement by peening, resulted in significantly lower yield and tensile strengths, with no overall gain in ductility compared to the standard WAAM condition.

In general, the yield strength in WAAM α-β titanium alloy with similar textures is inversely proportional to the α lath width but is more sensitive to the slip line length which is controlled by the colony size. In addition, it is also highly sensitive to the texture of the HCP α phase, relative to the loading direction, due to its strong slip anisotropy [8,54]. Nevertheless, peening did not change the α lath width or the matrix α morphology. Without post building heat treatment, the colony microstructure did not contribute to the strength increase observed. The β grain size was also large even in the peened alloys, and far larger than the slip path length which is controlled by the α colony size. Therefore, it can be argued that the observed increase in strength in the peened material is largely due to the weaker crystallographic texture, and, the spatial orientation of the α lamellae (Fig. 3). For example, transformation from a $< 001 >$ β//ND texture will produce many basal planes aligned nearly ideally for slip in both the vertical and horizontal loading directions, which are symmetrically related for an $< 001 >$ β//ND orientation. Thus, with the standard as built WAAM material, the WD and ND orientations tested are effectively "soft" directions, which leads to a lower yield strength in these loading directions compared to with the peened material that had a weak texture. This also impacts on the ductility as a higher yields stress tends to decrease the effective strain hardening rate that leads to earlier instability in tensile testing. However, further study is required to ascertain to what extent the degree of texture weakening and the orientation of α lath major axis contribute to the increase in yield strength and ultimate tensile strength.

Finally, the β annealed material had the lowest yield and tensile strengths, as shown in Figs. 5c, 5d, and Table 3. Compared to the peened condition, the yield strength was reduced by ~13 % for the horizontal samples and ~14 % for vertical samples. The primary reason for this is the lower cooling rate which results in a considerable increase in the α lath width, of 2.6 times (2.3 μm vs. 0.9 μm) as well as a change in microstructure to large single-variant colonies factors which leads to a much larger average slip line length, governed by the coarse single-variant colony size [48]. The lack of recovery in elongation with reduction in yield stress needs further investigation but is probably related to the thicker GB_α layer and greater plastic incompatibility across colony boundaries seen for this condition.

3.3. High cycle fatigue (HCF)

Fig. 6a shows the S-N data obtained from the rotating bending fatigue test. For comparison, test data of a forged bimodal and a forged lamellar microstructure from literature [26] are also shown in Fig. 6b. To compare with the current study, the literature data was converted from R ratio 0.1 to −1 using the Smith-Watson-Topper (SWT) method [55]. Despite considerable scatter in the S-N data, the as-built and hammer peened samples show higher fatigue strength than that of the β annealed, except a few data points due to scatter. This trend is consistent with that of the static tensile strength in the as-built and peened conditions (Fig. 5, Table 3). The influence of sample orientation on the fatigue strength is also shown in Fig. 6a. The as-built samples showed marginal anisotropic fatigue strength where the horizontal sample's strength was 50 MPa lower than that of the vertical samples. In the as-built condition, the majority of the α_{GB} are decorated with α colonies, indicating a strong crystallographic texture along the α_{GB}. In the horizontal samples, the α_{GB} is perpendicular to the loading direction, where the majority of the single-variant large α colonies are under the cyclic loading that greatly influence the crack initiation, thereby the fatigue life [56]. Hence, fatigue property anisotropy is found. Further detailed investigation of the role of microstructure and crystallographic texture along the α_{GB} is required to explain the marginal anisotropy between the horizontal and vertical samples in as-built and peened conditions.

After β annealing treatment, the increased α lath width led to a significant decrease in the fatigue strength, which is in line with the

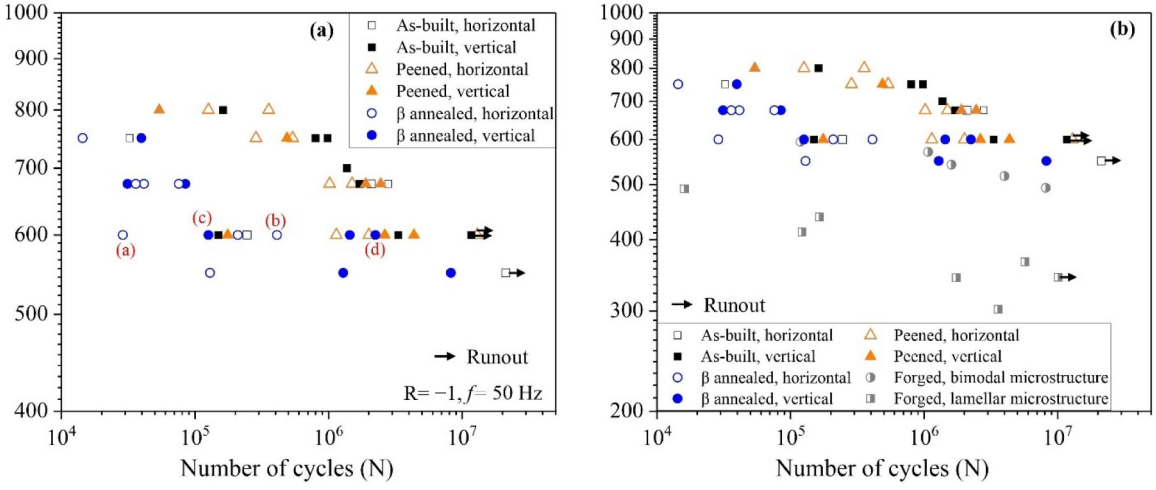

Fig. 6. (a) S-N data of three different conditions (as-built, hammer peened, and β annealed) tested at two material orientations. Marked (a, b, c, d) data correspond to fractography images in Fig. 7. (b) comparison with literature data (forged bimodal and forged lamella) [26]. Test runouts are indicted with an arrow.

reduction in static strength. Due to limited sample availability, it was not possible to determine the fatigue endurance strength at 10^7 cycles. However, the available fatigue test data suggests that the β annealed condition may have significantly decreased the fatigue endurance strength. Fig. 6 also shows that the β annealed specimens tested at a stress amplitudes of 600 and 550 MPa exhibited considerable scatter in the data. To understand this, fracture surface analysis was conducted on selected samples marked in Fig. 6a (a, b, c, d). The fractography images are presented in Fig. 7. First, there was no sign of any defects. All samples examined showed crack initiation from a microstructure feature, i.e., α lath, α colony, or α/β interface. Figs. 7a and 7b show two horizontal samples tested at the same stress amplitude 600 MPa. The fractography images revealed crack initiation from the region close to the specimen surface or subsurface with the presence of facets and crack propagation being characterized by the striations. Fig. 7a shows the shortest fatigue life, by almost a magnitude than the sample in Fig. 7b. A closer observation of Fig. 6a reveals that the crack might have initiated from a large colony, as shown by the large facet, which is characterised by cross-colony slip-band fracture [29]. Crack initiating from a large colony have lower resistance to cyclic slip, resulting in a shorter fatigue life.

β annealed vertical samples tested at 600 MPa are presented in Figs. 7c and 7d. The vertical samples showed similar crack initiation sources to the horizontal samples, with cracks initiating from surface or subsurface regions. Unlike the horizontal samples, distinct facets near the crack initiation site are not visible in the vertical samples. Therefore, it is difficult to identify the reasons for the scatter in the fatigue data. However, a previous study by the authors indicated that variations in the local microstructure and its crystallographic orientation around the crack initiation site are primary contributors to fatigue data scatter in WAAM built Ti64. For the same applied stress, samples with a higher distribution of the Schmid factor for the pyramidal slip system around the crack initiation site exhibited higher fatigue life [57]. In the current study, the strong crystallographic texture of the colony microstructure likely contributed to the scatter in the fatigue test data.

3.4. Fatigue crack growth rates

Fig. 8 shows logarithmic fatigue crack growth rate (FCGR, da/dN) vs. stress intensity factor range (ΔK) plots for the different microstructure conditions and crack orientations (vertical, ND-WD, and horizontal, WD-ND). Each test was repeated at least twice, and the results were consistent. The crack growth rate curves can be divided into three regions: the threshold and near threshold regime (da/dN < 10^{-9} m/cycle), the Paris law regime (da/dN = 10^{-9}-10^{-6} m/cycle), and the final fast crack growth and fracture regime (da/dN > 10^{-6} m/cycle). The following observations can be made by comparing the results for the individual material conditions in Fig. 8. Firstly, It can be seen from Fig. 8a-c that the sample orientation had little effect on the FCGR curves; i.e., with an orthogonal change in crack path from the WD-TD to the ND-TD plane the measured data is closely overlayed for all three material conditions, even with the standard as-built sample, which is surprising given the tensile ductility test results and its strong microstructure and texture anisotropy the sample orientation had little effect on the FCGR. In addition, the orientation of the test samples was also found to have a negligible effect on the threshold values for crack growth onset in all three conditions. Secondly, in the near threshold and low ΔK region (ΔK <10 MPa $m^{1/2}$), where the crack growth rate is expected to be controlled by smaller-scale microstructure characteristics [58,59], both the as-built and peened samples showed a similar threshold stress intensity factor range (ΔK_{th}) of ~2.5 MPa $m^{1/2}$. However, after post-build β annealing of the peened samples (for β grain refinement), ΔK_{th} increased by over 2.5 times to approximately 6 MPa $m^{1/2}$. The same ranking was observed in the Paris law regime (da/dN = 10^{-9}-10^{-6} m/cycle), with both the as-built standard and peened samples showing similar crack growth rates and the β-annealed condition having much lower crack growth rates, by approximately an order of magnitude.

In this region, the relation between the crack growth rate and stress intensity factor range can be described by the Paris law [60]:

$$\frac{da}{dN} = C(\Delta K)^m \tag{2}$$

where, C and m are material constants representing respectively the intersection of the curve to the y-axis and the slope of the logarithmic curves in Fig. 8.

Table 4 summarises the fitted Paris law constants for the three process conditions, between the crack growth rates of 10^{-8}–10^{-6} m/cycle, where a simple single-linear fit could be applied to the test results. Similar values for the intercept C and slope m are observed between the horizontal and vertical samples in each material condition, indicating little anisotropy between the two major orientations. However, the constant C was much lower for the β annealed samples, owing to the

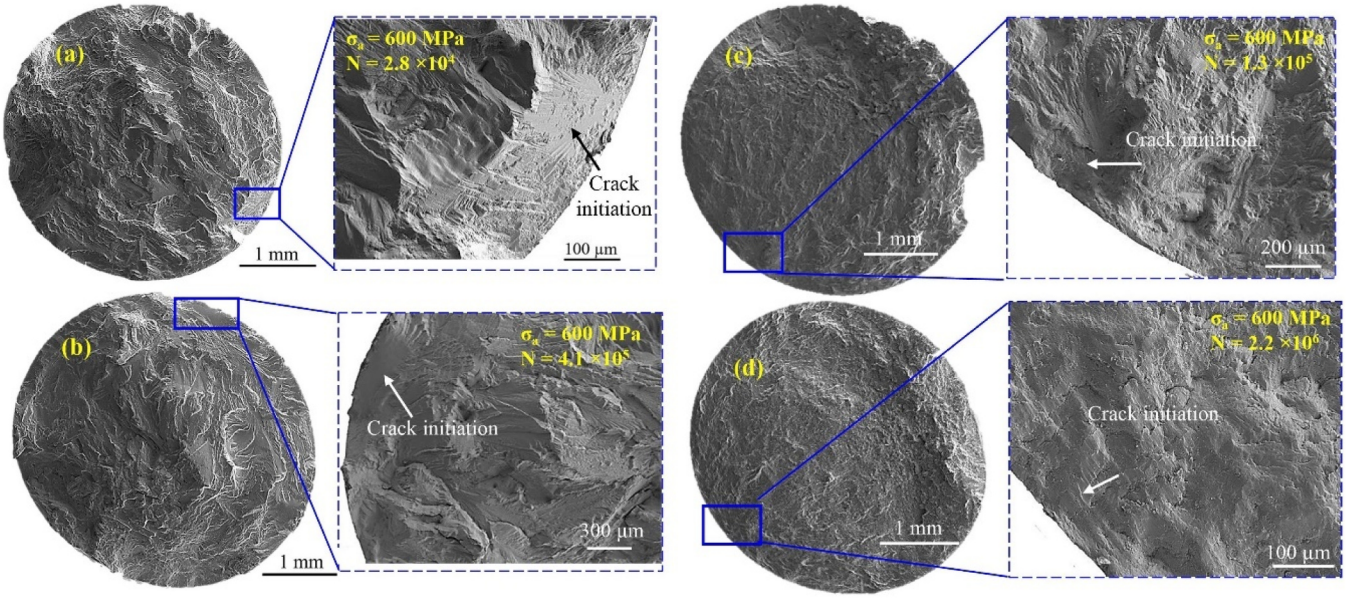

Fig. 7. Fracture surface analysis of selected β annealed samples as indicated in Fig. 5. (a) and (b): horizontal samples; (c) and (d) vertical samples.

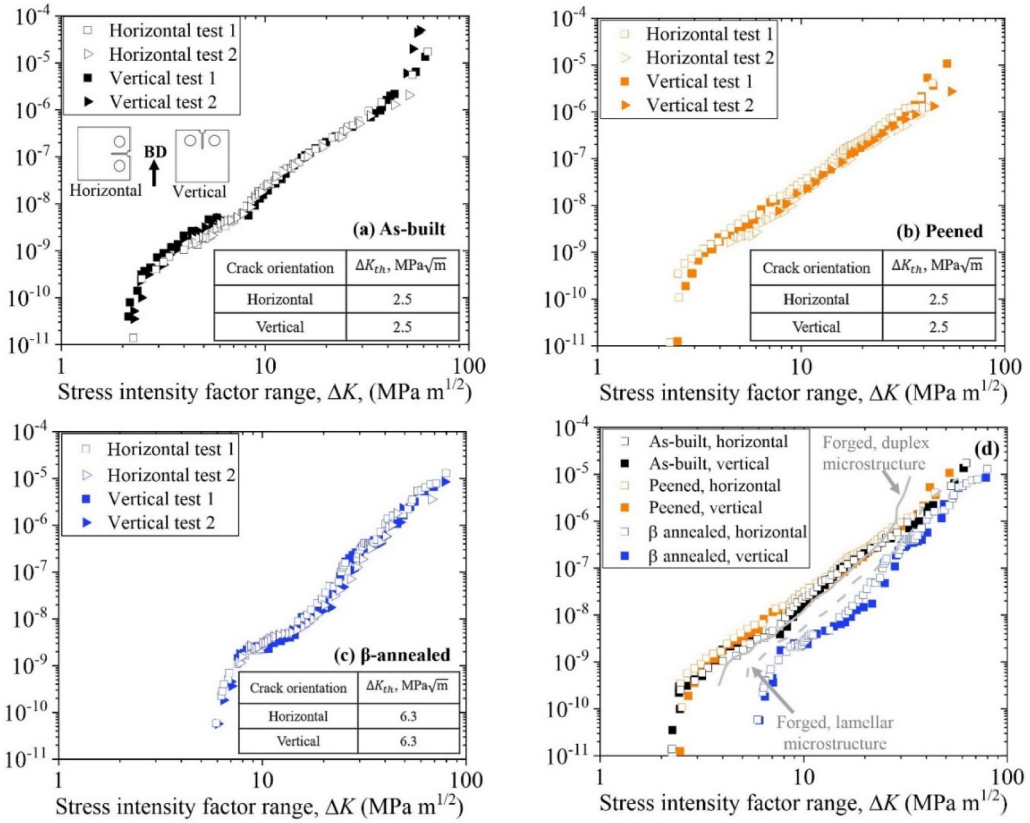

Fig. 8. Fatigue crack growth rate vs. stress intensity factor range for three conditions: (a) as-built, (b) peened, and (c) β annealed. (d) comparison of all three conditions and with a forged counterpart with dual phase microstructure and α/β lamellar colony microstructure [61].

Table 4
Paris law constant values based on Fig. 7 (averaged from 2 to 3 repeats).

Build condition	Sample orientation	Range of da/dN (m/cycle)	
		10^{-9} - 10^{-6}	
		C	m
As-built	Horizontal	1.31×10^{-11}	3.14
	Vertical	5.70×10^{-12}	3.43
Peened	Horizontal	2.54×10^{-11}	3.00
	Vertical	2.59×10^{-11}	2.91
β annealed	Horizontal	1.53×10^{-13}	4.13
	Vertical	2.79×10^{-13}	4.00

much lower crack growth rate compared to the materials without post-build heat treatment. The results of all the tests then tended to converge at high ΔK values prior to failure (i.e. longer crack lengths under constant amplitude loading).

It is worth noting that the test samples used in this study were extracted from a large wall. The extraction of much smaller samples would relieve the majority of the residual stresses in the deposited wall. We previously studied residual stresses in compact tension (CT) samples extracted from WAAM Ti64 walls [34], which showed negligible residual stress in the CT samples (average value of the maximum tensile stress was ~20 MPa) and the peak stress was at the sample's notch tip which was caused by the notch stress concentration effect. Therefore, residual stress in extracted samples has little or no influence on the test results presented in this paper; the properties measured can be regarded as the material's intrinsic properties. This is in contrast with the near net shape samples built by the powder bed fusion processes which contain considerable residual stresses.

3.5. The near threshold regime

The following discussion are based on the tests conducted under the constant amplitude loads; hence the governing parameter stress intensity factor increases with the growing crack length. Cracks are short in the near threshold regime, therefore fatigue crack growth rates are more sensitive to the condition of the fine scale microstructure. For longer cracks, the crack growth rate is more affected by the mechanical factors and mechanical shielding from crack closure. In the short crack regime, the crack growth rates are therefore less influenced by large scale features such as the relatively coarse β size in all the materials. In the case of the standard WAAM as-built and the peened material that were not post-build heat-treated, they both had very similar grain matrix microstructures which dominated the microstructure as the grain boundary α- single colony variant layers were thin due to the high cooling rate. This means that in these materials cracks mostly encounter the 'basket weave' grain matrix microstructure that consists of fine, tri-variant α colonies with fine lath widths that are formed due to the high cooling rate in the WAAM process. These tri-variant colonies do not have as strong a local microtexture as single-variant lamellar α colonies and this leads to a straighter crack path even for short cracks in the as-built samples. This near identical, finer and more crystallographically homogeneous transformation microstructure would therefore be expected to produce similar local slip characteristics at a crack tip and not deflect cracks onto specific crystal facets. Equally, they are not strongly influenced by long-length scale variability in the horizontal and vertical directions, arising from the grain structure and HAZ bands.

In comparison, the post-build β annealing treatment produces much coarser single α-variant colonies, with wider-spaced lamellar that will give a lower critical resolved shear stress but show much greater variability in their slip characteristics depending on the orientation of each colony. Slip transfer between laths, which all have the same orientation,

is relatively easy in such colonies as they behave essentially like a single grain. Thus, tend to deflect even short cracks much more strongly out of plane depending on the orientation of the easy basal and prismatic slip systems that can be activated in each colony encountered [30]. On average, this will lead to a lower effective resolved maximum crack tip stress intensity. For short cracks, the colony boundaries will therefore serve as stronger obstacles to crack propagation, thereby decreasing the crack growth rate [59].

3.6. Long cracks

Examples in Fig. 9 show the typical crack paths seen in the tests for the three different material conditions, starting from the crack starter notch to the crack length corresponding to a ΔK of ~ 7 MPa $m^{1/2}$. The relative topography of the fracture surfaces of the fractured samples is also evaluated and presented in Fig. 9. The as-built standard WAAM and the peened samples exhibited relatively planar crack paths (Figs. 9a, 9d and 9b, 9e). After β annealing a pronounced crack deflection and bifurcation (Figs. 9c, 9f) at the colony boundaries is observed that leading to higher resistance to crack propagation which was manifested by higher fracture surface roughness (Figs. 9c, 9f and 10). In contrast, Figs. 9a and 9b taken from the as-built samples show that both the cracks propagated in a relatively straight line with little deflection in macro-scale, despite that the cracks in horizontal test sample crossed the columnar grain boundaries. There was equally only weak crack deflection when the cracks propagated across the HAZ bands, seen in the vertical test samples.

In comparison, the β annealed samples (Figs. 9c, 9f) show evidence of much more irregular crack propagation with significant out of plane deflection, as well as bifurcation occurring at the coarse single α-variant colony boundaries present with this material condition. In long cracks, at low cyclic load ratio 0.1, this reduces the mode-I crack growth driving force, i.e., the effective value of the stress intensity factor range, due to crack closure caused by crack surface roughness and also cyclic plastic deformation, which led to much reduced crack growth rate [62]. This strong crack deflection at colony boundaries arises because of the single-variant colonies formed at low cooling rates. These colonies each contain α lamellae with a narrow spread from a single orientation. As a result, the slip transfer, leads to a more defined crack tip slip pattern and preferred planes of propagation within a given colony [30]. A similar behaviour has been widely reported for β annealed forged products [29], which are designed to increase the crack path roughness by developing coarse, single α-variant colony microstructures to increase damage tolerance. Our work has shown similar large differences in crack growth rates between β annealed and bimodal microstructures, although it has also been demonstrated that this difference reduces when crack closure effect is reduced when testing at higher R ratios [32].

In addition, when the crack is propagating perpendicular to the β grain boundary in the standard WAAM as-built condition, it only encounters a thin GB_α before quickly propagating again in the fine basketweave of the next parent β grain's matrix. As a result, the β grain boundaries do not give rise to relatively large crack deflections. Equally, although the HAZ bands will cause some local softening, this does not change the orientations of the α variants present which have simply coarsened due to the temperature rise, and therefore, the HAZ bands are also not as effective as deflecting crack as the β annealed single-colony microstructures. For the peened samples, the very weak texture and equiaxed β grain structure also means that there is little microstructural anisotropy to cause crack growth rates to vary in different growth directions. In comparison, post-build β annealed condition does not even contain HAZ bands and in terms of fatigue crack propagation it is essentially microstructurally isotropic.

The above observations are reflected in the surface height measurements presented in Fig. 10 obtained by mapping an area of 3 × 5 mm^2 at 5 mm distance from the crack starter notch tip, corresponding to a ΔK value range of 5–7 MPa $m^{1/2}$. The as-built and the peened samples both exhibited an average surface roughness S_A (arithmetical mean value of the measured surface) of approximately 10 μm (Figs. 10a, 10d, 10b, 10e), whereas the roughness value of the β annealed samples was more than doubled (10c, 10 f).

In summary, these results have clearly demonstrate the advantages of the β annealing treatment. The higher threshold value for ΔK will delay the onset of crack propagation by 2.5 times, and when combined with a 10 × lower crack growth rates, this heat treatment will be highly beneficial for extending the fatigue life, and help to meet the damage tolerance design criterion. This is due to the significantly delayed crack growth onset and much longer life spent in the Paris law crack growth regime, which also facilitates crack inspections.

4. Conclusions

The conventional coarse columnar β grain structure and transformation microstructure of the titanium alloy Ti6242, produced by wire arc directed energy deposition, was tailored by in-process peening and post-process β annealing. The effects on the microstructure, tensile, high cycle fatigue, and fatigue crack growth rate properties were studied for all three process conditions. Based on the reported findings, the following conclusions can be drawn.

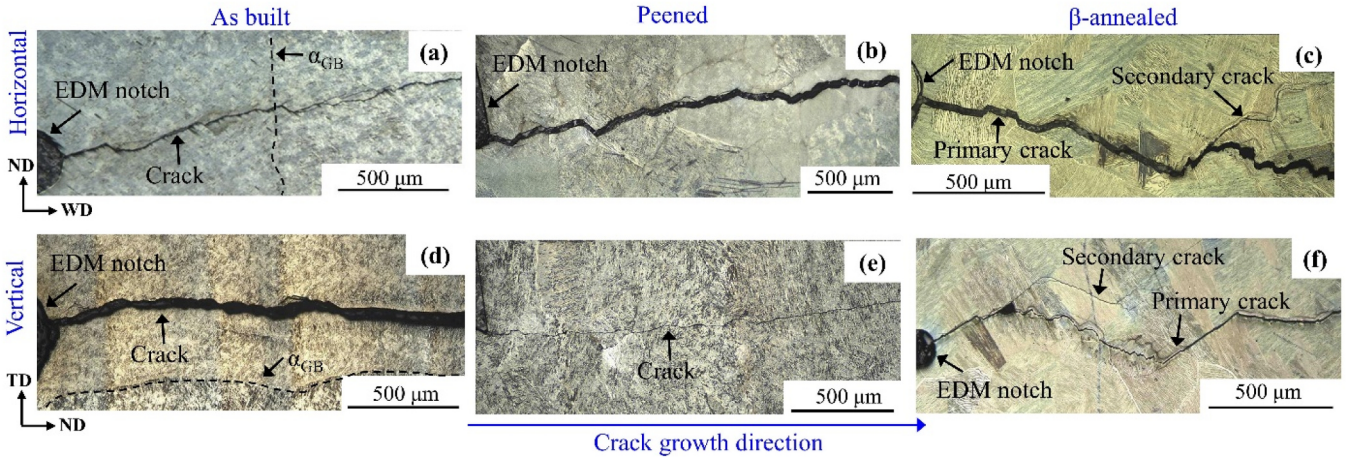

Fig. 9. Optical micrographs of the crack growth path near the EDM notch root in three different conditions: (a, b) standard WAAM as-built, (c, d) peened, (e, f) penned and β annealed. The notch root is on the left.

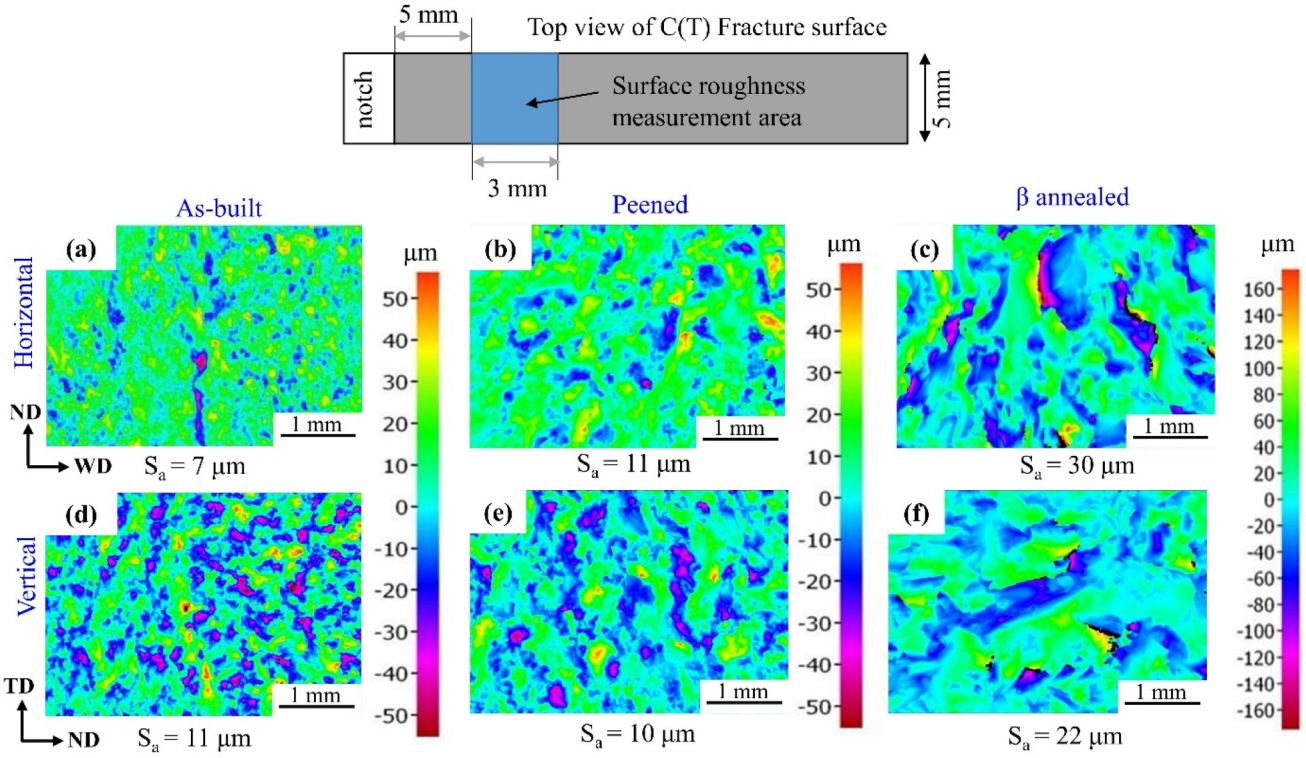

Fig. 10. Topographic height maps of fracture surfaces: (a, d) as-built, (b, e) peened, (c, f) peened + β annealed. Average value of surface roughness (S_A) is given beneath each map. Note the index range for (c, f) is 3 times greater than that for (a-d).

1. Interpass hammer peening has effectively refined the columnar prior β grain structure, typical in standard WAAM as-built material. This has resulted in a coarser yet improved equiaxed β grain structure with significantly reduced texture strength. Both the as-built and peened materials had fine multi-variant α colony (basketweave) transformation microstructures within the β grains. After the post-build β annealing, large single-variant lamellar α colonies were produced with a coarser α lath width.
2. In the standard as-built condition, the yield and tensile strengths were similar between major orientations. However, ductility in the horizontal direction was lower than the vertical direction due to the slip concentration in thin GB_α single-variant colonies, leading to earlier fracture. The slip concentration was the cause of strong ⟨001⟩β // ND texture in columnar β grains.
3. Interpass peening has reduced the anisotropy in the ductility and increased the yield strength by 10 % due to weaker crystallographic texture and α lamellae orientation. Isotropic tensile properties were maintained after the post-build β annealing. Although the yield strength was slightly decreased in the annealed condition due to increased α lath width, strength values are comparable to the standard WAAM as-built condition.
4. High cycle fatigue performance followed the same ranking as the tensile strength, which can be attributed to the similar α lath width in the as-built and peened materials. Fatigue life was decreased after β annealing due to larger α lath width and colony microstructure. Data scatter has prevented us from assessing the effect of sample orientation.
5. For each of the three build conditions, fatigue crack growth rate is fairly isotropic between the two orthogonal planes. Multi-variant α colonies and similar α lath width in the as-built and peened samples have resulted in comparable crack growth rates. In contrast, post-build β annealing, which created large single-variant colonies, has reduced crack growth rates by an order of magnitude and increased the threshold stress intensity factor range by 2.5 times due to significant crack path deviation and branching.
6. Grain refinement through interpass deformation and microstructure tailoring via post-deposition β annealing have enhanced fatigue crack growth resistance for high damage tolerance while maintaining adequate static strength and fatigue durability.

CRediT authorship contribution statement

Williams Stewart: Writing – review & editing, Resources, Funding acquisition. **Prangnell Philip B:** Writing – review & editing, Resources, Funding acquisition. **Syed Abdul Khadar:** Writing – review & editing, Methodology, Conceptualization. **Zakir Farhana:** Writing – original draft, Investigation, Formal analysis. **Davis Alec E:** Writing – review & editing, Investigation, Formal analysis. **Zhang Xiang:** Writing – review & editing, Supervision, Resources, Methodology, Funding acquisition, Conceptualization. **Sahu Vivek K:** Writing – review & editing, Investigation, Formal analysis. **Biswal Romali:** Resources. **Caballero Armando E:** Resources.

Declaration of Competing Interest

The authors declare that they have no known competing financial interests or personal relationships that could have appeared to influence the work reported in this paper.

Acknowledgements

We would like to thank the UK Engineering and Physical Science Research Council (EPSRC) for supporting this research through the "New Wire Additive Manufacturing (NEWAM)" programme grant (EP/R027218/1). The authors would also like to thank Steve Damms and Colin Thorneycraft from Coventry University for their assistance with sample extraction and machining.

Data Availability

The author has shared the link to the data in the manuscript.

References

[1] E.W.C.G. Welsch, R. Boyer, Materials Properties Handbook: Titanium Alloys, ASM International, Metals Park (OH), 1994.

[2] J.C.W.G. Lütjering, High Temperature Alloys, in: G. Lütjering, J.C. Williams (Eds.), Titanium, Springer Berlin Heidelberg, Berlin, Heidelberg, 2007, pp. 259–282, https://doi.org/10.1007/978-3-540-73036-1_6.

[3] R. Huang, M. Riddle, D. Graziano, J. Warren, S. Das, S. Nimbalkar, J. Cresko, E. Masanet, Energy and emissions saving potential of additive manufacturing: the case of lightweight aircraft components, J. Clean. Prod. 135 (2016) 1559–1570, https://doi.org/10.1016/J.JCLEPRO.2015.04.109.

[4] B. Blakey-Milner, P. Gradl, G. Snedden, M. Brooks, J. Pitot, E. Lopez, M. Leary, F. Berto, A. du Plessis, Metal additive manufacturing in aerospace: a review, Mater. Des. 209 (2021) 110008, https://doi.org/10.1016/J.MATDES.2021.110008.

[5] S.W. Williams, F. Martina, A.C. Addison, J. Ding, G. Pardal, P. Colegrove, Wire + Arc additive manufacturing, Mater. Sci. Technol. 32 (2016) 641–647, https://doi.org/10.1179/1743284715Y.0000000073.

[6] A.E. Davis, A.E. Caballero, R. Biswal, S. Williams, P.B. Prangnell, Comparison of microstructure refinement in wire-arc additively manufactured Ti–6Al–2Sn–4Zr–2Mo–0.1Si and Ti–6Al–4V built with inter-pass deformation, Metall. Mater. Trans. A 53 (2022) 3833–3852, https://doi.org/10.1007/s11661-022-06811-1.

[7] F. Wang, S. Williams, P. Colegrove, A.A. Antonysamy, Microstructure and mechanical properties of wire and arc additive manufactured Ti-6Al-4V, Metall. Mater. Trans. A 44 (2013) 968–977, https://doi.org/10.1007/s11661-012-1444-6.

[8] A.K. Syed, X. Zhang, A. Caballero, M. Shamir, S. Williams, Influence of deposition strategies on tensile and fatigue properties in a wire + arc additive manufactured Ti-6Al-4V, Int J. Fatigue 149 (2021), https://doi.org/10.1016/j.ijfatigue.2021.106268.

[9] M.J. Bermingham, D. Kent, H. Zhan, D.H. Stjohn, M.S. Dargusch, Controlling the microstructure and properties of wire arc additive manufactured Ti-6Al-4V with trace boron additions, Acta Mater. 91 (2015) 289–303, https://doi.org/10.1016/j.actamat.2015.03.035.

[10] S. Mereddy, M.J. Bermingham, D. Kent, A. Dehghan-Manshadi, D.H. StJohn, M. S. Dargusch, Trace carbon addition to refine microstructure and enhance properties of additive-manufactured Ti-6Al-4V, JOM 70 (2018) 1670–1676, https://doi.org/10.1007/s11837-018-2994-x.

[11] J. Han, G. Zhang, X. Chen, Y. Cai, Z. Luo, X. Zhang, Y. Su, Y. Tian, High strength Ti alloy fabricated by directed energy deposition with in-situ Cu alloying, J. Mater. Process Technol. 310 (2022) 117759, https://doi.org/10.1016/J.JMATPROTEC.2022.117759.

[12] J.R. Kennedy, A.E. Davis, A. Caballero, A. Garner, J. Donoghue, S. Williams, J. Zollinger, E. Bouzy, E.J. Pickering, P.B. Prangnell, Isomorphic grain inoculation in Ti-6Al-4V during additive manufacturing, Mater. Lett.: X 8 (2020) 100057, https://doi.org/10.1016/j.mlblux.2020.100057.

[13] J.R. Kennedy, A.E. Davis, A.E. Caballero, S. Williams, E.J. Pickering, P. B. Prangnell, The potential for grain refinement of Wire-Arc Additive Manufactured (WAAM) Ti-6Al-4V by ZrN and TiN inoculation, Addit. Manuf. 40 (2021) 101928, https://doi.org/10.1016/J.ADDMA.2021.101928.

[14] A.E. Davis, J. Wainwright, V.K. Sahu, D. Dreelan, X. Chen, J. Ding, T. Flint, S. Williams, P.B. Prangnell, Achieving a columnar-to-equiaxed transition through dendrite twinning in high deposition rate additively manufactured titanium Alloys, Metall. Mater. Trans. A 55 (2024) 1765–1787, https://doi.org/10.1007/s11661-024-07388-7.

[15] J. Wainwright, S. Williams, J. Ding, Refinement of Ti-6Al-4V prior-β grain structure in the as-deposited condition via process control during wire-direct energy deposition, Addit. Manuf. 74 (2023) 103712, https://doi.org/10.1016/J.ADDMA.2023.103712.

[16] J. Donoghue, A.A. Antonysamy, F. Martina, P.A. Colegrove, S.W. Williams, P. B. Prangnell, The effectiveness of combining rolling deformation with wire–arc additive manufacture on β-grain refinement and texture modification in Ti–6Al–4V, Mater. Charact. 114 (2016) 103–114, https://doi.org/10.1016/j.matchar.2016.02.001.

[17] L. Neto, S. Williams, J. Ding, J. Hönnige, F. Martina, Mechanical properties enhancement of additive manufactured Ti-6Al-4V by machine hammer peening, in: S. Itoh, S. Shukla (Eds.), Advanced Surface Enhancement, Springer Singapore, Singapore, 2020, pp. 121–132.

[18] F. Martina, StewartW. Williams, P. Colegrove, Improved microstructure and increased mechanical properties of additive manufacture produced TI-6AL-4V by interpass cold rolling (Austin, United States), : 24th Int. Solid Free. Fabr. Symp. . - Addit. Manuf. Conf. (2013) 490–496.

[19] X. Tian, Y. Zhu, C.V.S. Lim, J. Williams, R. Boyer, X. Wu, K. Zhang, A. Huang, Isotropic and improved tensile properties of Ti-6Al-4V achieved by in-situ rolling in direct energy deposition, Addit. Manuf. 46 (2021) 102151, https://doi.org/10.1016/J.ADDMA.2021.102151.

[20] C. Fleißner-Rieger, T. Pfeifer, T. Jörg, T. Kremmer, M. Brabetz, H. Clemens, S. Mayer, Selective laser melting of a Near-α Ti6242S alloy for high-performance automotive parts, Adv. Eng. Mater. 23 (2021) 2001194, https://doi.org/10.1002/adem.202001194.

[21] A.R.Riccardo Casati, Gabriele Boari, M. Vedani, Effect of annealing temperature on microstructure and high-temperature tensile behaviour of Ti-6242S alloy produced by Laser Powder Bed Fusion, Eur. J. Mater. 1 (2021) 72–83, https://doi.org/10.1080/26889277.2021.1997341.

[22] M. Lopez, C. Pickett, E. Arrieta, L.E. Murr, R.B. Wicker, M. Ahlfors, D. Godfrey, F. Medina, Effects of Postprocess Hot Isostatic Pressing Treatments on the Mechanical Performance of EBM Fabricated TI-6Al-2Sn-4Zr-2Mo, Materials 13 (2020), https://doi.org/10.3390/ma13112604.

[23] H. Fan, S. Yang, Effects of direct aging on near-alpha Ti–6Al–2Sn–4Zr–2Mo (Ti-6242) titanium alloy fabricated by selective laser melting (SLM), Mater. Sci. Eng.: A 788 (2020) 139533, https://doi.org/10.1016/J.MSEA.2020.139533.

[24] Z. Zhu, F.L. Ng, H.L. Seet, S.M.L. Nai, Tailoring the microstructure and mechanical property of laser powder bed fusion fabricated Ti–6Al–2Sn–4Zr–2Mo via heat treatment, J. Alloy. Compd. 895 (2022) 162648, https://doi.org/10.1016/J.JALLCOM.2021.162648.

[25] G.Q. Wu, C.L. Shi, W. Sha, A.X. Sha, H.R. Jiang, Effect of microstructure on the fatigue properties of Ti–6Al–4V titanium alloys, Mater. Des. (1980-2015) 46 (2013) 668–674, https://doi.org/10.1016/J.MATDES.2012.10.059.

[26] M. Hagiwara, T. Kitashima, S. Emura, Relationship between microstructures, facet morphologies at the high-cycle fatigue (HCF) crack initiation site, and HCF strength in Ti-6242S, Mater. Sci. Eng.: A 727 (2018) 43–50, https://doi.org/10.1016/J.MSEA.2018.04.043.

[27] T.K. Heckel, A. Guerrero Tovar, H.-J. Christ, Fatigue of the Near-Alpha Ti-Alloy Ti6242, Exp. Mech. 50 (2010) 483–489, https://doi.org/10.1007/s11340-009-9238-5.

[28] J. Yu, K. Su, X. Lin, H. Tan, Q. Yan, Y. Tang, W. Huang, High-temperature mechanical performance of directed energy deposited Ti6242S alloy, Mater. Sci. Eng.: A 850 (2022) 143526, https://doi.org/10.1016/J.MSEA.2022.143526.

[29] R.K. Nalla, R.O. Ritchie, B.L. Boyce, J.P. Campbell, J.O. Peters, Influence of microstructure on high-cycle fatigue of Ti-6Al-4V: Bimodal vs. lamellar structures, Metall. Mater. Trans. A 33 (2002) 899–918, https://doi.org/10.1007/s11661-002-0160-z.

[30] A.L. Pilchak, R.E.A. Williams, J.C. Williams, Crystallography of fatigue crack initiation and growth in fully lamellar Ti-6Al-4V, Metall. Mater. Trans. A 41 (2010) 106–124, https://doi.org/10.1007/s11661-009-0064-2.

[31] H. Zhou, H. Liu, D. Yi, Y. Xiao, X. Zhao, J. Wang, Q. Gao, Effect of α phase on fatigue crack growth of Ti-6242 alloy, J. Iron Steel Res. Int. 24 (2017) 811–822, https://doi.org/10.1016/S1006-706X(17)30121-8.

[32] N. Verdhan, D.D. Bhende, R. Kapoor, J.K. Chakravartty, Effect of microstructure on the fatigue crack growth behaviour of a near-α Ti alloy, Int J. Fatigue 74 (2015) 46–54, https://doi.org/10.1016/J.IJFATIGUE.2014.12.013.

[33] M. Hagiwara, T. Kitashima, S. Emura, Relationship between microstructures, facet morphologies at the high-cycle fatigue (HCF) crack initiation site, and HCF strength in Ti-6242S, Mater. Sci. Eng.: A 727 (2018) 43–50, https://doi.org/10.1016/J.MSEA.2018.04.043.

[34] B. Ahmad, X. Zhang, H. Guo, M.E. Fitzpatrick, L.M.S.C. Neto, S. Williams, Influence of Deposition Strategies on Residual Stress in Wire + Arc Additive Manufactured Titanium Ti-6Al-4V, Met. (Basel) 12 (2022), https://doi.org/10.3390/met12020253.

[35] ASTM E112-13, Standard Test Methods for Determining Average Grain Size, in: 2021.

[36] P.S. Davies, B.P. Wynne, W.M. Rainforth, M.J. Thomas, P.L. Threadgill, Development of Microstructure and Crystallographic Texture during Stationary Shoulder Friction Stir Welding of Ti-6Al-4V, Metall. Mater. Trans. A 42 (2011) 2278–2289, https://doi.org/10.1007/s11661-011-0606-2.

[37] ASTM E647-15e1, Standard Test Method for Measurement of Fatigue Crack Growth Rates, in: ASTM International, West Conshohocken, PA, 2015.

[38] A.A. Antonysamy, J. Meyer, P.B. Prangnell, Effect of build geometry on the β-grain structure and texture in additive manufacture of Ti6Al4V by selective electron beam melting, Mater. Charact. 84 (2013) 153–168, https://doi.org/10.1016/j.matchar.2013.07.012.

[39] J. Wang, X. Lin, J. Wang, H. Yang, Y. Zhou, C. Wang, Q. Li, W. Huang, Grain morphology evolution and texture characterization of wire and arc additive manufactured Ti-6Al-4V, J. Alloy. Compd. 768 (2018) 97–113, https://doi.org/10.1016/J.JALLCOM.2018.07.235.

[40] J. Caballero, Alec E. Davis, P. Prangnell, Microstructural characterisation and mechanical properties of Ti-5Al-5V-5Mo-3Cr built by wire and arc additive manufacture, Philos. Mag. 102 (2022) 2256–2281, https://doi.org/10.1080/14786435.2022.2113470.

[41] A.E. Davis, J.R. Kennedy, J. Ding, P.B. Prangnell, The effect of processing parameters on rapid-heating β recrystallization in inter-pass deformed Ti-6Al-4V wire-arc additive manufacturing, Mater. Charact. 163 (2020) 110298, https://doi.org/10.1016/J.MATCHAR.2020.110298.

[42] B. Vrancken, L. Thijs, J.P. Kruth, J. Van Humbeeck, Heat treatment of Ti6Al4V produced by Selective Laser Melting: Microstructure and mechanical properties, J. Alloy. Compd. 541 (2012) 177–185, https://doi.org/10.1016/J.JALLCOM.2012.07.022.

[43] S.L. Lu, Z.J. Zhang, R. Liu, Z. Qu, B. Wang, X.H. Zhou, J. Eckert, Z.F. Zhang, Prior β grain evolution and phase transformation of selective laser melted Ti6Al4V alloy during heat treatment, J. Alloy. Compd. 914 (2022) 165235, https://doi.org/10.1016/J.JALLCOM.2022.165235.

[44] A.L. Pilchak, G.A. Sargent, S.L. Semiatin, Early Stages of Microstructure and Texture Evolution during Beta Annealing of Ti-6Al-4V, Metall. Mater. Trans. A 49 (2018) 908–919, https://doi.org/10.1007/s11661-017-4444-8.

[45] D. Lunt, A. Ho, A. Davis, A. Harte, F. Martina, J. Quinta da Fonseca, P. Prangnell, The effect of loading direction on strain localisation in wire arc additively

manufactured Ti–6Al–4V, Mater. Sci. Eng.: A 788 (2020) 139608, https://doi.org/10.1016/J.MSEA.2020.139608.
[46] S.M. Kelly, S.L. Kampe, Microstructural evolution in laser-deposited multilayer Ti-6Al-4V builds: Part I. Microstructural characterization, Metall. Mater. Trans. A 35 (2004) 1861–1867, https://doi.org/10.1007/s11661-004-0094-8.
[47] A. Ho, H. Zhao, J.W. Fellowes, F. Martina, A.E. Davis, P.B. Prangnell, On the origin of microstructural banding in Ti-6Al4V wire-arc based high deposition rate additive manufacturing, Acta Mater. 166 (2019) 306–323, https://doi.org/10.1016/J.actamat.2018.12.038.
[48] G. Lütjering, Influence of processing on microstructure and mechanical properties of (α+β) titanium alloys, Mater. Sci. Eng.: A 243 (1998) 32–45, https://doi.org/10.1016/S0921-5093(97)00778-8.
[49] S. Liu, Y.C. Shin, Additive manufacturing of Ti6Al4V alloy: a review, Mater. Des. 164 (2019) 107552, https://doi.org/10.1016/j.matdes.2018.107552.
[50] M.J. Donachie. Titanium, A technical guide, 2nd edition, ASM International, Metals Park (OH), 2000.
[51] L. Thijs, M.L. Montero Sistiaga, R. Wauthle, Q. Xie, J.-P. Kruth, J. Van Humbeeck, Strong morphological and crystallographic texture and resulting yield strength anisotropy in selective laser melted tantalum, Acta Mater. 61 (2013) 4657–4668, https://doi.org/10.1016/j.actamat.2013.04.036.
[52] B.E. Carroll, T.A. Palmer, A.M. Beese, Anisotropic tensile behavior of Ti–6Al–4V components fabricated with directed energy deposition additive manufacturing, Acta Mater. 87 (2015) 309–320, https://doi.org/10.1016/J.ACTAMAT.2014.12.054.
[53] S. Cao, L. Meng, H. Liu, Y. Zou, A. Smith, X. Wu, J. Donoghue, R. Thomas, M. Preuss, D. Lunt, Role of microstructure heterogeneity on deformation behaviour in additive manufactured Ti-6Al-4V, Mater. (Oxf.) 26 (2022) 101636, https://doi.org/10.1016/J.MTLA.2022.101636.
[54] A.E. Davis, C.I. Breheny, J. Fellowes, U. Nwankpa, F. Martina, J. Ding, T. Machry, P.B. Prangnell, Mechanical performance and microstructural characterisation of titanium alloy-alloy composites built by wire-arc additive manufacture, Mater. Sci. Eng.: A 765 (2019) 138289, https://doi.org/10.1016/J.MSEA.2019.138289.
[55] K.N. Smith, A Stress-Strain Function for the Fatigue of Metals, J. Mater. (1970) 767–778. ⟨https://api.semanticscholar.org/CorpusID:222375816⟩.
[56] M. Shamir, A.K. Syed, V. Janik, R. Biswal, X. Zhang, The role of microstructure and local crystallographic orientation near porosity defects on the high cycle fatigue life of an additive manufactured Ti-6Al-4V, Mater. Charact. 169 (2020) 110576, https://doi.org/10.1016/j.matchar.2020.110576.
[57] M. Shamir, A.K. Syed, V. Janik, R. Biswal, X. Zhang, The role of microstructure and local crystallographic orientation near porosity defects on the high cycle fatigue life of an additive manufactured Ti-6Al-4V, Mater. Charact. 169 (2020), https://doi.org/10.1016/j.matchar.2020.110576.
[58] Y. Xie, M. Gao, F. Wang, C. Zhang, K. Hao, H. Wang, X. Zeng, Anisotropy of fatigue crack growth in wire arc additive manufactured Ti-6Al-4V, Mater. Sci. Eng.: A 709 (2018) 265–269, https://doi.org/10.1016/J.MSEA.2017.10.064.
[59] Y. Wang, R. Chen, X. Cheng, Y. Zhu, J. Zhang, H. Wang, Effects of microstructure on fatigue crack propagation behavior in a bi-modal TC11 titanium alloy fabricated via laser additive manufacturing, J. Mater. Sci. Technol. 35 (2019) 403–408, https://doi.org/10.1016/J.JMST.2018.10.031.
[60] P. Paris, F. Erdogan, A Critical Analysis of Crack Propagation Laws, J. Basic Eng. 85 (1963) 528–533, https://doi.org/10.1115/1.3656900.
[61] W. Shen, W.O. Soboyejo, A.B.O. Soboyejo, An investigation on fatigue and dwell-fatigue crack growth in Ti–6Al–2Sn–4Zr–2Mo–0.1Si, Mech. Mater. 36 (2004) 117–140, https://doi.org/10.1016/S0167-6636(03)00035-8.
[62] S. Leuders, M. Thöne, A. Riemer, T. Niendorf, T. Tröster, H.A. Richard, H.J. Maier, On the mechanical behaviour of titanium alloy TiAl6V4 manufactured by selective laser melting: Fatigue resistance and crack growth performance, Int J. Fatigue 48 (2013) 300–307, https://doi.org/10.1016/J.IJFATIGUE.2012.11.011.

Microstructure tailoring of a wire-arc DED processed Ti6242 alloy for high damage tolerance performance

Zakir, Farhana

2025-05-05

Zakir F, Syed AK, Zhang X, et al., (2025) Microstructure tailoring of a wire-arc DED processed Ti6242 alloy for high damage tolerance performance. Additive Manufacturing, Volume 105, May 2025, Article number 104785

https://doi.org/10.1016/j.addma.2025.104785